Wave-cloud dynamics in the atmospheric boundary layer

By A. Balakrishna, H. Fu†, P. Moin AND M. E O'Neill‡

We study gravity waves incident on low-altitude clouds with numerical simulation. The gravity waves are introduced as an imposed vertical momentum forcing upon a rigorously constructed stationary stratocumulus-topped boundary layer. The forcing form recovers the internal gravity wave dispersion relation in a dry framework, and baseline parameters of the forcing are estimated from satellite measurement. The effect of the forcing amplitude on the boundary layer in terms of breakup propensity as well as the modulation of the energetics and turbulent stress state is explored.

1. Introduction

Stratocumulus clouds are low-altitude clouds that extensively cover Earth's subtropical and midlatitude oceans. Consequently, stratocumulus play an important role in setting the radiative-exchange budget of the atmosphere by cooling the surface via reflection of sunlight (Wood 2012). Given the role stratocumulus clouds play in regulating the climate, it is important to study the factors that lead to their breakup.

In this study, we are interested in how external forcings influence the stratocumulus-topped boundary layer (STBL). Previous modeling work in this vein involved varying the background aerosol concentration profile, which can delay breakup timing (Goren *et al.* 2019). Thermodynamic forcings have also been explored via the modulation of the base state moisture or temperature profiles (Bohnert 1994; Wang *et al.* 2010) in addition to climatic forcings like doubling carbon dioxide concentrations (Schneider *et al.* 2019).

A relatively unexplored type of perturbation mechanism is atmospheric gravity waves (AGW) traveling through the STBL. These waves transfer momentum and energy to the global circulation, exhibit a broadband spectrum in terms of their wavelength and period, and are generated by a variety of sources in the atmosphere (Achatz *et al.* 2024). Recent satellite observations (e.g., Allen *et al.* 2013) revealed trains of horizontally propagating wave packets that led to pockets of open cells (POCs) in the cloud deck. Large-eddy simulation (LES) is an attractive paradigm to study this problem, as it allows mean convective and turbulence effects to be resolved while also providing a computationally cost-effective tool to explore the wave parameter space. Initial LES of this case has shown that fractional diurnal period waves augmented precipitation in the cloud leading to cellularization (Jiang & Wang 2012), whereas successive waves were shown to clear the deck due to the instigating of dry air entrainment and attenuated longwave cooling (Connolly *et al.* 2013).

We seek to build upon the aforementioned through additional parametric study of gravity waves incident on stratocumulus. The forced waves will instead be in the short wavelength/period regime ($\mathcal{T} \sim \mathcal{O}(10)$ min; Jia *et al.* 2019) rather than a globally felt

† School of the Atmospheric Sciences, Nanjing University, China
‡ Department of Physics, University of Toronto, Canada

subsidence forcing as in Jiang & Wang (2012) and Connolly *et al.* (2013). Additionally, we systematically control for nonstationary effects like the diurnal cycle by constructing a novel radiative-convective equilibrium (RCE) framework for the STBL, and ensure sufficient resolution of the inversion to capture entrainment scales (Bretherton *et al.* 1999). Characterization of the STBL turbulence through detailed examination of the energy budgets and turbulent stress state among the various wave forcings tested merits further study of this potential breakup regime.

2. Methodology

2.1. *Model setup*

We perform cloud-permitting LES with Cloud Model 1 (CM 1, Bryan & Fritsch 2002). The governing equations for mass conservation and momentum in a compressible framework in tensor notation are

$$\frac{\partial \rho^*}{\partial t^*} + \frac{\partial}{\partial x_j^*}(\rho^* u_j^*) = 0, \tag{2.1}$$

$$\frac{\partial u_i^*}{\partial t^*} + u_j^* \frac{\partial u_i^*}{\partial x_j^*} = -c_p \theta_\rho^* \frac{\partial \pi'}{\partial x_i^*} - 2\epsilon_{ijk}\Omega_j(u_k^* - u_k^{*G}) + \frac{g}{\theta_{\rho 0}^*}\theta_\rho'^* \delta_{i3} + T_i^* + W_i^* + N_i^*. \tag{2.2}$$

Here c_p is the dry air specific heat; Ω is Earth's rotation rate; ρ^* is the density of the moist parcel; u_i^* is the velocity in the three ordinate directions; $\theta_\rho^* = \theta^*(1 + q_v/\epsilon)/(1 + q_v + q_l)$ is the density potential temperature as a function of the potential temperature and specific humidities for vapor and liquid; $\pi = (p^*/p_o)^{R/c_p}$ is the Exner function; T_i^* is the subgrid-scale stress (SGS) term; W_i^* is the contribution due to the large-scale subsidence field; and lastly, N_i^* represents a sponge layer term. Primes denote deviations from the base state (indicated by a subscript 0) and asterisked quantities indicate dimensional variables. See the CM 1 documentation for a detailed description of the prognostic moisture, temperature and pressure equations and the modified Deardorff (1980) SGS model utilized in this study.

A few key forcings are necessary to maintain the structure of the STBL (Balakrishna *et al.* 2024). A mean wind of $u_o = 7$ m/s and $v_o = -5.5$ m/s in the boundary layer was chosen based on observation (Stevens *et al.* 2005) and enforced as the geostrophic component, u_k^{*G} in the Coriolis term of Eq. (2.2). Next, to model the impact of circulation on the boundary layer, a large-scale subsidence velocity is prescribed

$$w_{LS}^* = -Dz^*, \tag{2.3}$$

where $D > 0$ is a constant indicative of the bulk divergence. We choose $D = 3.75 \times 10^{-6}$ s^{-1} and this velocity is added as a source term,

$$W_i^* = w_{LS}^* \left(\frac{\partial \phi}{\partial z^*}\delta_{i1} + \frac{\partial \phi}{\partial z^*}\delta_{i2} \right) \tag{2.4}$$

for $\phi = [u^*, v^*, \theta^*, q_v, q_l]$ all in line with the process described in Stevens *et al.* (2005). The initial state is quite susceptible to strong convective warming, so an adequate radiative cooling model is needed to reach an equilibrium. The radiation model we employ is a modification to that presented in Stevens *et al.* (2005),

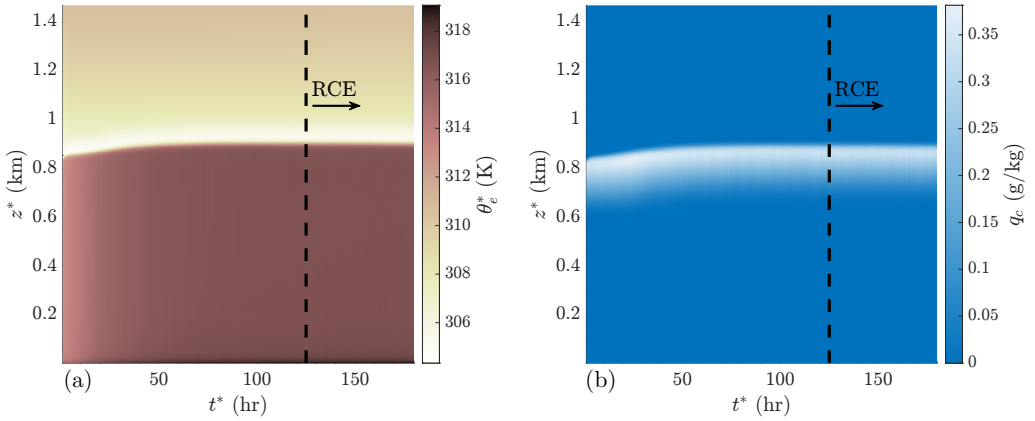

FIGURE 1. Spatiotemporal contour of (a) equivalent potential temperature and (b) cloud–condensate specific humidity for the current setup. The onset of radiative-convective equilibrium is denoted by the black dashed lines in both panels.

$$F_{rad} = F_o \exp\left[-\kappa \int_{z^*}^{\infty} \rho^* r_l \, dz^*\right] + F_1 \exp\left[-\kappa \int_0^{z^*} \rho^* r_l \, dz^*\right] \tag{2.5}$$

where the first two terms accounting for the cloud-top cooling and cloud base warming are retained. Following Balakrishna *et al.* (2024), we prescribe a newtonian cooling term with a constant timescale $\tau_c = 3$ hr, but with the modification to constrain this term to the region above the inversion layer, representing free troposphere cooling

$$\dot{Q}_\theta^* = \frac{\theta'^*}{\tau_c}. \tag{2.6}$$

We initialize the STBL based on the Dynamics and Chemistry of Marine Stratocumulus (DYCOMS-II) field campaign–derived (Stevens *et al.* 2003, 2005) potential temperature and vapor specific humidity. The domain is configured like a channel with $L_x = L_y = 4\pi$ km and $L_z = 1.5$ km to support a wide range of wavelengths with potential for horizontal propagation. A grid of $\Delta x = \Delta y = 30.0$ m and $\Delta z = 5$ m leads to approximately 5 grid points across the inversion, commensurate with the entrainment-resolving guidelines given in Bretherton *et al.* (1999).

Boundary conditions in the horizontal directions are periodic. The bottom boundary condition is a neutral log law wall model for the ocean surface with a constant sea surface temperature of 292.5 K along with corresponding surface sensible and latent heat fluxes. The top boundary condition is a free slip condition with a sponge layer that relaxes the flow field toward the horizontal average in the upper 300 m to prevent spurious downward wave reflection. Figure 1 shows the equivalent potential temperature and cloud condensate vertical profiles as a function of time. Stationarity in the STBL is attained after $t = 125$ hr according to the criterion presented in Balakrishna *et al.* (2024).

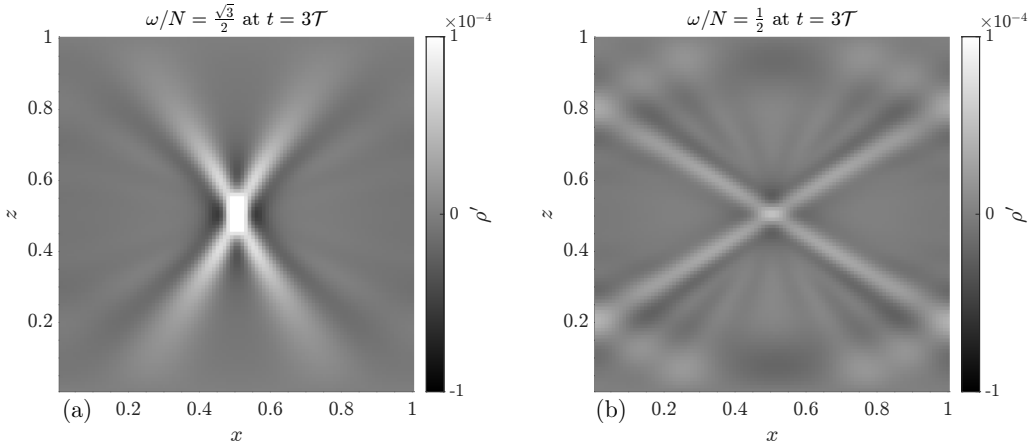

FIGURE 2. Dry, uniformly stratified setup with Eq. (2.7) imposed in the center of the domain. Dimensionless density perturbation contour of (a) a forcing whose relative frequency yields a measured wave vector angle of 31.9°, and (b) 60.0° which agrees quite well with linear theory values of 30° and 60°, respectively. Both contours are shown after three periods of forcing. N denotes the background buoyancy frequency.

2.2. *Gravity wave forcing*

Our gravity wave model is a third imposed forcing acting directly on the vertical momentum equation

$$\mathcal{F}_i^* = Ae^{-\left(\frac{x^*-x_c}{a}\right)^2-\left(\frac{z^*-z_c}{b}\right)^2}\sin(-\omega t^*)\delta_{i3} \tag{2.7}$$

where A is the amplitude; a, b are the half-widths in the x and z directions; ω is the temporal frequency; and (x_c, z_c) is the center location of the forcing. The form of Eq. (2.7) is inspired by a plane wave packet; the Gaussian term also ensures a smooth spatial decay in the forcing. Each parameter constitutes a member of the analysis sweep in this study as A dictates the strength of the forcing, choice of (x_c, z_c) exposes the forcing to differing regions of stratification in the STBL and ω implicitly sets the spectrum of wavelengths that are excited by the forcing. The half-widths are chosen to constrain the forcing below the inversion so as to not energize the nonturbulent free troposphere. In the limit of $a, b \to \infty$ and oscillatory period of $\sim$ 1 hr, the forcing form approaches the (global) subsidence forcing in Connolly *et al.* (2013). The use of Eq. (2.7) is further validated, as this forcing captures the linear dispersion relation of internal gravity waves in a dry, stably stratified setup (Vallis 2017)

$$\omega/N = \cos\alpha, \tag{2.8}$$

where α is the angle the wavevector (perpendicular to the wave group) makes with the horizontal. Figure 2 illustrates the density perturbation contours for two choices of ω/N. The angle of the phase lines for each case agrees well with the expected α in Eq. (2.8).

2.3. *Proposed nondimensionalization*

It is helpful to understand the relative magnitude of these forcings in the context of a nondimensionalized momentum equation. We take a velocity scale $U \sim \sqrt{u_o^2 + v_o^2}$, length scale $L \sim \overline{z}_i$, where $\overline{z}_i$ is the average inversion height defined by the $q_t = q_l + q_v = 8$ g/kg isoline (Stevens *et al.* 2005), temperature scale $\theta_s \sim \theta_{\rho 0}$, the Coriolis parameter f to normalize Ω^* and a vertical convective overturning timescale $t_s \sim \overline{z}_i/U$. Applying the

Run ID	$\mathcal{A} = A\overline{z}_i/U^2$	$z_c/\overline{z}_i$	ω/ω_{ref}	$t_f\omega/2\pi$
Base	0.11	0.5	1	1
A1	0.56	0.5	1	1
A2	1.13	0.5	1	1
A3	1.98	0.5	1	1
A4	2.82	0.5	1	1

TABLE 1. Gravity wave forcing parameter sweep runs.

normalization in this manner leads to the dimensionless momentum equations

$$\frac{\partial u_i}{\partial t} + u_j\frac{\partial u_i}{\partial x_j} = -\mathrm{Ja}_m\theta_\rho\frac{\partial \pi'}{\partial x_i} - \frac{2}{\mathrm{Ro}}\epsilon_{ijk}\Omega_j(u_k - u_k^G) + \frac{1}{\mathrm{Fr}^2}\theta'_\rho\delta_{i3} + \frac{\overline{z}_i}{U^2}\left[\mathcal{F}^*\delta_{i3} + T_i^* + N_i^* + W_i^*\right], \quad (2.9)$$

with the three nondimensional parameters being the Froude number (Fr), Rossby number (Ro) and what we term a moist Jakob number (Ja_m) defined as

$$\mathrm{Ja}_m = \frac{c_p\theta_{\rho 0}}{U^2}, \quad (2.10)$$

$$\mathrm{Ro} = \frac{U}{f\overline{z}_i}, \quad (2.11)$$

and

$$\mathrm{Fr} = \frac{U}{\sqrt{g\overline{z}_i}}. \quad (2.12)$$

Table 1 summarizes the simulations performed in terms of the nondimensional amplitude, vertical location, frequency and number of periods forced. The experimental run Base has wave parameters whose values are observationally grounded. We define a reference period of $\mathcal{T}_{ref} = 1.5$ hr (such that $\omega_{ref} = 2\pi/\mathcal{T}_{ref}$), which is the same as the satellite-derived measurements in Connolly *et al.* (2013). Choice of this forcing's amplitude is based on an order-of-magnitude analysis. In Connolly *et al.* (2013), the peak forced subsidence velocity occurred at z_i with a corresponding value of $\mathcal{O}(10^{-1})$ m/s. Assuming the acceleration timescale is also $t_s = \mathcal{O}(10^1)$ s, this leads to a dimensional amplitude estimate of 10^{-2} m/s^2.

Here, we focus on the effect of the forcing amplitude. Note that all runs have an active forcing time of one integer period. Each forcing is applied during the RCE state (Figure 1); a horizontal sponge is additionally applied 300 m from each boundary to prevent lateral reflections toward the domain interior. Figure 3 illustrates a Hovmöller diagram of the forcing for case A1 and A3 in Table 1, reflecting the location and intensity of the various forcings. All experiments utilized $a/\overline{z}_i = 1.12$, $x_c/\overline{z}_i = 3.36$, $b/\overline{z}_i = 0.223$. Note that $\overline{z}_i = 894$ m in the RCE state of the STBL.

3. Amplitude effect

A simple statistic to compare the various cases in the forcing parameter sweep is the percentage of cloud cleared during the simulation time period. A region deficit of cloud

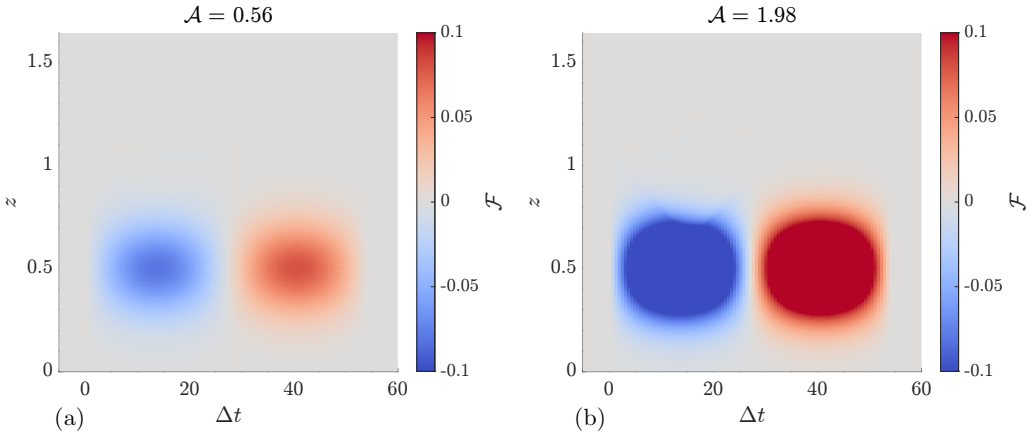

FIGURE 3. Spatiotemporal contour for the amplitude simulations: (a) A1 and (b) A3.

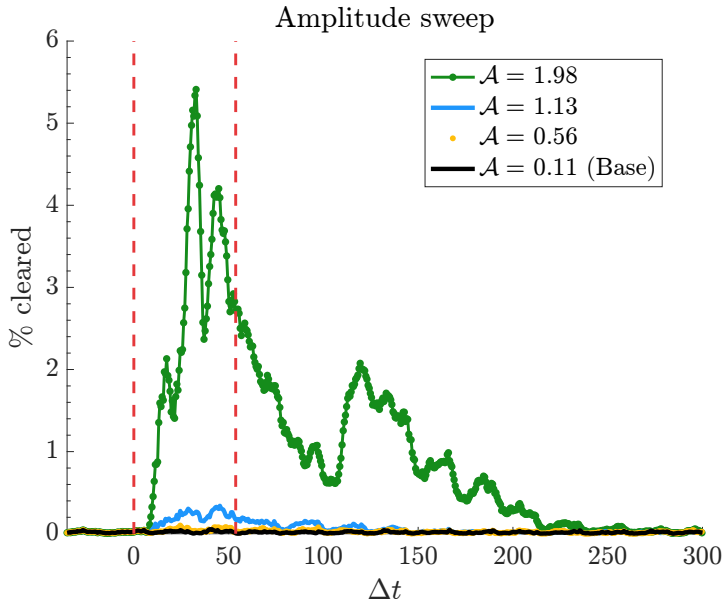

FIGURE 4. Total cloud-cleared percentage as a function of time since the forcing onset for Base, A1, A2 and A3. The red dashed lines denote the time window in which the forcings were active.

is defined as having a liquid water path (LWP) less than 10^{-3} kg/m^2 where

$$\mathrm{LWP} = \int_0^\infty \rho^* r_l \, dz^*. \tag{3.1}$$

Figure 4 shows the time trace of cleared cloud relative to the forcing onset for the four cases in which the amplitude was varied. The observationally derived forcing (Base) led to no change in the cloud deck, as did a forcing whose amplitude was five times larger. Some weak signature of breakup is observed for $\mathcal{A} = 1.13$, which supports the nondimensionalization choice to derive Eq. (2.9): an $O(1)$ term was necessary to overcome the RCE balance. Increasing the amplitude further to $\mathcal{A} = 1.98$ leads to a pronounced signal and a

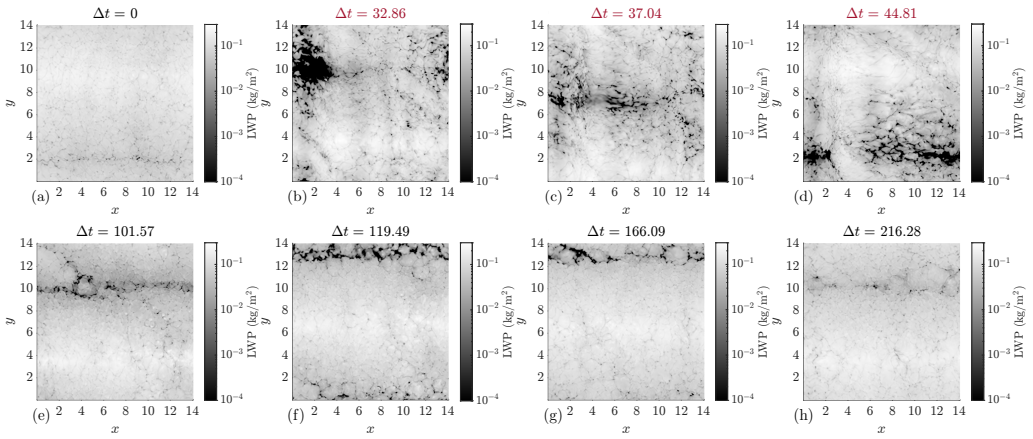

FIGURE 5. Snapshots of LWP through time for case A3. Red plot titles indicate active forcing. Panel (b) is at the max clearing time, and (f) is at the peak "rebound" point after the forcing ceased, as seen in Figure 4.

peak breakup of nearly 6%. Curiously for A3, there is a second peak within $\Delta t = 5$ of the first peak at $\Delta t = 32$ before the recovery of the cloud deck after the forcing ceased. This second peak is not correlated with the zero-crossing of the forcing nor with the time trace of entrainment velocity, suggesting the behavior is likely attributable to additional nonlinear effects between the forcing and STBL. All four cases exhibit an equilibration back to the stationary state by $\Delta t = 300$, though the STBL under the largest amplitude forcing experiences another slight uptick in clearing near $\Delta t = 120$. After this uptick, there is a decaying oscillation-like behavior with a period of approximately $(L_x/\overline{z}_i)\,\mathrm{sec}(v_o/u_o)$, which is a domain recirculation time due to the periodic boundary conditions.

Figure 5 illustrates the full liquid water path field through time for A3. Panels (b), (c), and (f) show the LWP field at the three local maxima in Figure 4 where open cellular structures are initially clustered together. As time progresses, these open cells are advected to the southeast by the mean winds forming a horizontal line of POCs. After $\Delta t > 200$, open cellular convection transitions back to its closed cell counterpart.

3.1. *Turbulent state*

To better understand how the turbulent state is modulated by the forcing, we analyze budgets of the turbulent kinetic energy (TKE) equation

$$\underbrace{\frac{\partial}{\partial t}\left(\frac{1}{2}\overline{u_i'u_i'}\right)}_{\partial k/\partial t} = \underbrace{-\overline{u_i'u_j'}\frac{\partial \overline{u}_i}{\partial x_j}}_{\mathcal{P}} \underbrace{-\mathrm{Ja}_m\overline{u_i'\theta_\rho}\frac{\partial \pi'}{\partial x_i}}_{\Pi} \underbrace{-\overline{u}_j\frac{\partial}{\partial x_j}\left(\frac{1}{2}\overline{u_i'u_i'}\right) - \overline{u_j'\frac{\partial}{\partial x_j}\left(\frac{1}{2}u_i'u_i'\right)}}_{\tau} + \underbrace{\frac{1}{\mathrm{Fr}^2}\overline{u_i'\theta_\rho'}\delta_{i3}}_{\mathcal{B}}$$
$$+ \frac{\overline{z}_i}{U^2}\Big(\underbrace{\overline{u_i'T_i'^*} + \overline{u_i'N_i'^*}}_{\varepsilon} + \underbrace{\overline{u_i'\mathcal{F}'^*}\delta_{i3}}_{\Lambda}\Big). \quad (3.2)$$

The terms on the right-hand side are production ($\mathcal{P}$), pressure correlation (Π), combined mean and turbulent transport of TKE (τ), buoyancy generation/destruction ($\mathcal{B}$), dissipation (ϵ) and forcing injection (Λ). Note that we are neglecting the TKE due to subsidence as it is quite small relative to the other terms. Figure 6 shows the various budget terms from Eq. (3.2) evolving through time and as a function of the vertical for

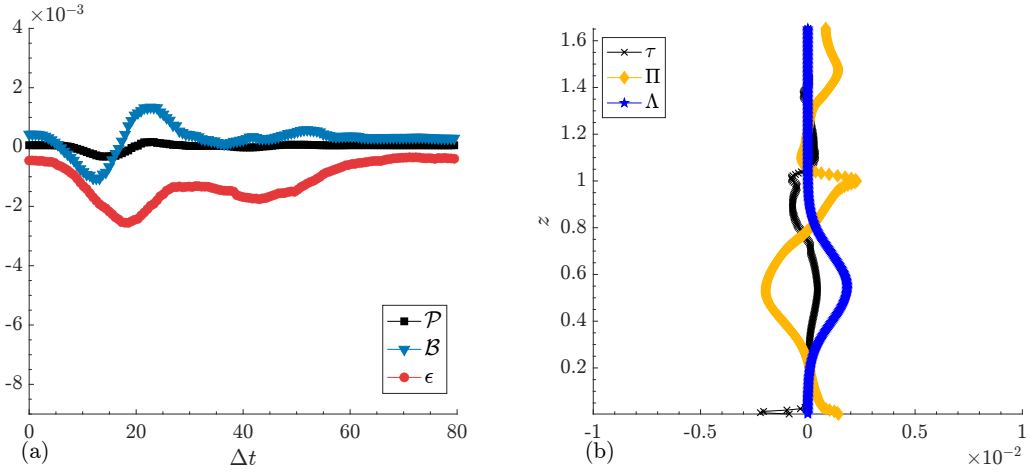

FIGURE 6. TKE budget terms as a function of (a) time upon volume averaging and (b) z averaging over three forcing periods for A3.

case A3. In terms of the temporal plot, the shape of the buoyancy curve has the same structure as the imposed forcing; Figure 6(a) illustrates $\mathcal{B}$ undergoing one periodic oscillation. The buoyancy term plays a dual role in draining TKE to the mean kinetic energy for the first 20 time units, while energizing the turbulence in the latter part of the active forcing window. Turbulent dissipation lags the buoyancy term. The magnitude of $\mathcal{P}$ is less than half of $\mathcal{B}$. Weak shear production is primarily due to local vertical gradients in u and v near the surface; the forcing does not introduce significant horizontal gradients to augment other components of $\mathcal{P}$.

How TKE is distributed throughout the boundary layer can be understood by analyzing the transport and pressure correlation terms shown in Figure 6(b). Peak injection of TKE via the forcing at $z \sim 0.5$ is mediated by the pressure correlation transferring energy back to the mean flow and returning that energy to the turbulence near the inversion, $z \sim 1$. The combined transport term is largely opposite in sign to Π.

3.2. *Transition to patchy regime*

As seen above, increasing the forcing wave energy leads to more transient clearing. A question that remains is if there exists a minimum forcing amplitude that pushes the STBL away from RCE in a quasi-permanent manner. Figure 7 shows one such case where $\mathcal{A} = 2.82$. Not only does the cloud deck dramatically clear during active forcing seen in Figure 7(b–d), this is sustained after the forcing ceases. The LWP at $\Delta t = 404.48$ exemplifies the complete transition to sparse areas of spotlike patches of cloud. The largest amplitude tested that did not result in this new cloud state was $\mathcal{A} = 2.40$, so more investigation is necessary if $\mathcal{A} = 2.82$ is indeed a critical value.

Lastly, since the gravity wave forcing is introduced as a source term for solely the vertical momentum, it is also useful to characterize the anisotropy of the flow. This is quantified by the Reynolds stress anisotropy tensor

$$b_{ij} = \frac{\overline{u_i' u_j'}}{\overline{u_k' u_k'}} - \frac{1}{3}\delta_{ij}. \tag{3.3}$$

Figure 8 is a Lumley triangle visualization where ξ and η represent invariants of b_{ij},

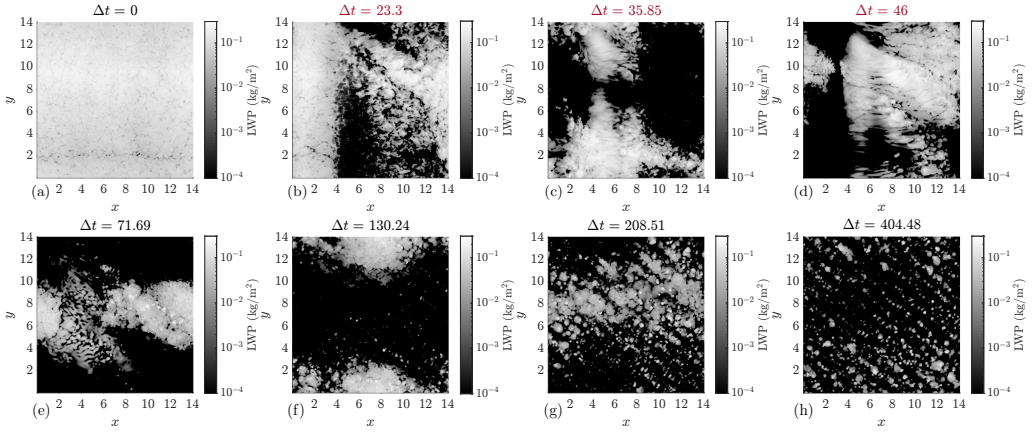

FIGURE 7. Snapshots of LWP through time for case A4. Again, the red panel titles denote active forcing.

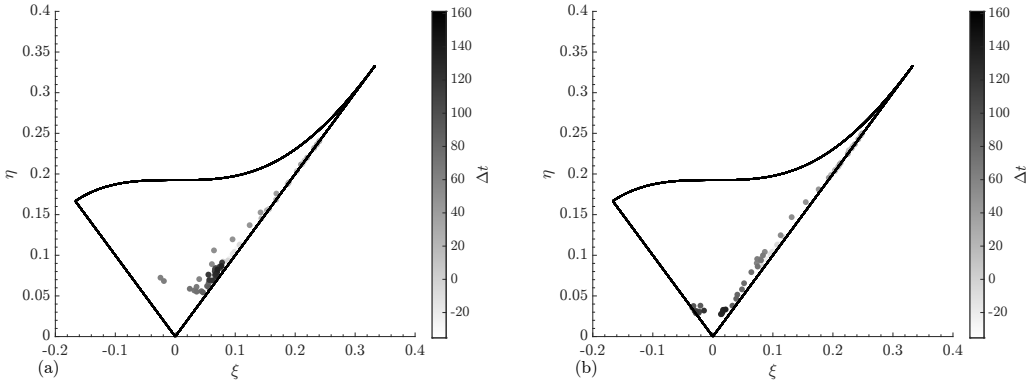

FIGURE 8. Lumley triangle diagram for case (a) A3 and (b) A4. Circular markers show progression through time from white to black.

which can be expressed in terms of its eigenvalues (Pope 2000). The $(0, 0)$ point represents the isotropic limit whereas the right (left) corner indicate that one (two) diagonal components of the Reynolds stress are dominant (Yi & Koseff 2022). Overbars in Eq. (3.3) denote a full volume average in this case. The black lines of the triangle bound the possible turbulent states. In the RCE state and during the onset of forcing, both A3 and A4 start near the bottom left of the $\eta = +\xi$ axisymmetric line. As time progresses, the (η, ξ) coordinate approaches the top right so-called rodlike limit of b_{ij}. After the forcing ceases around $t \sim 50$, the A3 stress state converges near the RCE point as expected. However, the A4 state appears to traverse toward the $\eta = -\xi$ disklike leg before settling again near the rodlike leg, but closer to the isotropic limit.

4. Conclusions

We have explored the effect of a gravity wave forcing on the stratocumulus-topped boundary layer with LES. The forcing took the form of a plane wave and acted as a source term for the vertical momentum equation. In the limit of a dry, shear-free configuration, the forcing recovers the linear dispersion relation of internal gravity waves.

In order to ascertain the impact of the forcing itself, we constructed a novel radiative-convective equilibrium framework for the STBL by introducing a newtonian relaxation term in the area above the cloud that represents free troposphere cooling. The degree of stationarity is measured by the equivalent potential temperature. Initializing the STBL with field campaign–derived profiles from Stevens *et al.* (2005) leads to the onset of RCE after 125 hours of model spin-up.

The characteristics of a nominal forcing were estimated from satellite measurements of these wave packets in the southeastern Pacific (Allen *et al.* 2013; Connolly *et al.* 2013). From this baseline we focused on the impact of the forcing amplitude. Only forcings where $\mathcal{A} > 1$ led to any large-scale change in the LWP, which lends support for the proposed nondimensional scales of the average inversion height and bulk base state velocity. Increasing the amplitude to an apparent critical value (A4) also led to a largely broken cloud deck that did not recover back to RCE, unlike the other experiments (within the total simulation time window).

Lastly, we looked at turbulent kinetic energy budgets as well as the degree of anisotropy across all the forced simulations. Investigation of the $\mathcal{A} = 1.98$ case revealed the dominance of the buoyancy generation term relative to shear production. A Lumley triangle analysis also revealed the possible stress states the STBL experiences upon the onset of forcing and well after the forcing passes. The anisotropy largely straddled the rodlike leg for A3 and A4, but the latter tended further toward the isotropic limit.

Future studies with this novel STBL RCE-wave framework should also consider the impact of varying the period, vertical location and chromaticity of the forcing. It would also be illuminating to further dissect the flow field into a mean ($\overline{u}_i$), fluctuating (u_i') and wave components ($\tilde{u}_i$) to better understand the interplay between the background and forcing modes superposed on the turbulent state. In order to construct $\tilde{u}_i$, one must identify a singular, distinct period to define a phase average (Hussain & Reynolds 1970). Performing this decomposition may also prove insightful to understand the forcing amplitude threshold that separates a temporary broken regime from one where the clouds are persistently patchy.

Acknowledgments

A.B. acknowledges support from a National Science Foundation Graduate Research Fellowship (Grant Number DGE-1656518). The authors acknowledge computing resources provided by the Stanford Research and Computing Center and G. Bryan for maintaining CM 1.

REFERENCES

Achatz, U., Alexander, M. J., Becker, E., Chun, H.-Y., Dörnbrack, A., Holt, L., Plougonven, R., Polichtchouk, I., Sato, K., Sheshadri, A. *et al.* 2024 Atmospheric gravity waves: Processes and parameterization. *J. Atmos. Sci.* **81**, 237–262.

Allen, G., Vaughan, G., Toniazzo, T., Coe, H., Connolly, P., Yuter, S. E., Burleyson, C. D., Minnis, P. & Ayers, J. K. 2013 Gravity-wave-induced perturbations in marine stratocumulus. *Quart. J. Roy. Meteor. Soc.* **139**, 32–45.

Balakrishna, A., Fu, H., Moin, P. & O'Neill, M. 2024 Radiative-convective equi-

librium in the stratocumulus-topped boundary layer. *Annual Research Briefs,* Center for Turbulence Research pp. 53–64.

Bohnert, M. J. 1994 *A numerical investigation of cloud-topped planetary boundary layers*. Ph.D. Thesis, Stanford University.

Bretherton, C. S., MacVean, M. K., Bechtold, P., Chlond, A., Cotton, W. R., Cuxart, J., Cuijpers, H., Khairoutdinov, M., Kosovic, B., Lewellen, D. *et al.* 1999 An intercomparison of radiatively driven entrainment and turbulence in a smoke cloud, as simulated by different numerical models. *Quart. J. Roy. Meteor. Soc.* **125**, 391–423.

Bryan, G. H. & Fritsch, J. M. 2002 A benchmark simulation for moist nonhydrostatic numerical models. *Mon. Weather Rev.* **130**, 2917–2928.

Connolly, P. J., Vaughan, G., Cook, P., Allen, G., Coe, H., Choularton, T. W., Dearden, C. & Hill, A. 2013 Modelling the effects of gravity waves on stratocumulus clouds observed during VOCALS-UK. *Atmos. Chem. Phys.* **13**, 7133–7152.

Deardorff, J. 1980 Stratocumulus-capped mixed layers derived from a three-dimensional model. *Bound. Layer. Meteor.* **18**, 495–527.

Goren, T., Kazil, J., Hoffmann, F., Yamaguchi, T. & Feingold, G. 2019 Anthropogenic air pollution delays marine stratocumulus breakup to open cells. *Geophys. Res. Lett.* **46**, 14135–14144.

Hussain, A. K. M. F. & Reynolds, W. C. 1970 The mechanics of an organized wave in turbulent shear flow. *J. Fluid Mech.* **41**, 241–258.

Jia, M., Yuan, J., Wang, C., Xia, H., Wu, Y., Zhao, L., Wei, T., Wu, J., Wang, L., Gu, S.-Y. *et al.* 2019 Long-lived high-frequency gravity waves in the atmospheric boundary layer: observations and simulations. *Atmos. Chem. Phys.* **19**, 15431–15446.

Jiang, Q. & Wang, S. 2012 Impact of gravity waves on marine stratocumulus variability. *J. Atmos. Sci.* **69**, 3633–3651.

Pope, S. B. 2000 *Turbulent Flows*, 3rd ed. Cambridge University Press.

Schneider, T., Kaul, C. & Pressel, K. 2019 Possible climate transitions from breakup of stratocumulus decks under greenhouse warming. *Nature* pp. 163–167.

Stevens, B., Lenschow, D. H., Vali, G., Gerber, H., Bandy, A., Blomquist, B., Brenguier, J.-L., Bretherton, C., Burnet, F., Campos, T. *et al.* 2003 Dynamics and chemistry of marine stratocumulus—DYCOMS-II. *Bull. Amer. Meteor. Soc.* **84**, 579–594.

Stevens, B., Moeng, C.-H., Ackerman, A. S., Bretherton, C. S., Chlond, A., de Roode, S., Edwards, J., Golaz, J.-C., Jiang, H., Khairoutdinov, M. *et al.* 2005 Evaluation of large-eddy simulations via observations of nocturnal marine stratocumulus. *Mon. Weather Rev.* **133**, 1443–1462.

Vallis, G. K. 2017 *Atmospheric and Oceanic Fluid Dynamics*. Cambridge University Press.

Wang, H., Feingold, G., Wood, R. & Kazil, J. 2010 Modelling microphysical and meteorological controls on precipitation and cloud cellular structures in Southeast Pacific stratocumulus. *Atmos. Chem. Phys.* **10**, 6347–6362.

Wood, R. 2012 Stratocumulus clouds. *Mon. Weather Rev.* **140**, 2373–2423.

Yi, Y. R. & Koseff, J. R. 2022 Dynamics and energetics underlying mixing efficiency in homogeneous stably stratified turbulence. *Phys. Rev. Fluids* **7**, 084801.